Atmos. Meas. Tech. Discuss., 5, 5753–5785, 2012
www.atmos-meas-tech-discuss.net/5/5753/2012/
doi:10.5194/amtd-5-5753-2012

Atmospheric Measurement Techniques Discussions

Application of linear polarized light for the discrimination of frozen and liquid droplets in ice nucleation experiments

T. Clauss[1], **A. Kiselev**[1,2], **S. Hartmann**[1], **S. Augustin**[1], **S. Pfeifer**[1], **D. Niedermeier**[1], **H. Wex**[1], **and F. Stratmann**[1]

[1]Institute for Tropospheric Research, Permoser Str. 15, 04318 Leipzig, Germany
[2]Institute for Meteorology and Climate Research, Karlsruhe Institute of Technology, Postfach 3640, 76021 Karlsruhe, Germany

Received: 22 July 2012 – Accepted: 1 August 2012 – Published: 20 August 2012

Correspondence to: T. Clauss (tina.clauss@tropos.de)

Published by Copernicus Publications on behalf of the European Geosciences Union.

Abstract

We report on the development and test results of the new optical particle counter TOPS-Ice (Thermostabilized Optical Particle Spectrometer for the detection of Ice particles). The instrument uses measurements of the depolarized component of light scattered by single particles into the near-forward direction ($42.5^{\circ} \pm 12.7^{\circ}$) to distinguish between spherical and non-spherical particles. This approach allows the differentiation between liquid water droplets (spherical) and ice particles (non-spherical) having similar volume equivalent sizes and therefore can be used to determine the fraction of frozen droplets in a typical immersion freezing experiment. We show that the numerical simulation of the light scattering on non-spherical particles (ellipsoids in random orientation) with account for the actual scattering geometry used in the instrument supports the validity of the approach, even though the cross polarized component of the light scattered by spherical droplets is not vanishing in this scattering angle. For the separation of the ice particle mode from the liquid droplet mode, we use the width of the pulse detected in the depolarization channel instead of the pulse height. Exploiting the intrinsic relationship between pulse height and pulse width for Gaussian pulses allows us to calculate the fraction of frozen droplets even if the liquid droplet mode dominates the particle ensemble. We present test results obtained with TOPS-Ice in the immersion freezing experiments at the laminar diffusion chamber LACIS (Leipzig Aerosol Cloud Interaction Simulator) and demonstrate the excellent agreement with the data obtained in the same experiment with a different optical instrument. Finally, the advantages of using the cross-polarized light measurements for the differentiation of liquid and frozen droplets in the realistic immersion freezing experiments are discussed.

1 Introduction

Ice particles in clouds affect strongly the cloud dynamics and radiative properties and therefore the Earth's climate (Cantrell and Heymsfield, 2005). Whereas in high

AMTD
5, 5753–5785, 2012

stratospheric clouds, ice forms mostly by direct deposition from the vapor phase onto solid aerosol particles, ice particles in mixed-phase tropospheric clouds tend to form by freezing of liquid droplets condensed on the preexisting solid particles called ice nuclei (IN). In this context, an important freezing mechanism under atmospheric conditions is immersion freezing (Ansmann et al., 2008; de Boer et al., 2011; Connolly et al., 2009; Hoose et al., 2010; Wiacek et al., 2010), where supercooled droplets with immersed insoluble particles freeze. These particles lower the free energy barrier associated with the formation of an ice germ of critical size in the supercooled liquid water and therefore dramatically enhance the rate of supercooled droplet freezing leading to higher onset temperature of ice formation (which is approximately −38 °C for homogeneous freezing of supercooled water droplets (Pruppacher and Klett, 1997)). However, the physical and chemical properties of aerosol particles that are responsible for their ability to serve as heterogeneous ice nuclei are not entirely understood. Among other qualities, the affinity of the crystalline structure of mineral dust to the crystalline structure of ice, the presence of the OH radicals on the surface of organic IN, or a special protein on the surface of biological particles are considered. To elucidate these unknowns, laboratory studies involving well characterized reference IN are required.

Among others, the ongoing research in this field is done in the expansion cloud chambers (AIDA, Wagner et al., 2009) and ice nucleation chambers of the continuous flow diffusion type (LACIS, Stratmann et al., 2004; Hartmann et al., 2011, CFDC, Rogers, 1988, FINCH, Bundke et al., 2008, ZINC, Stetzer et al., 2008), where liquid droplets with immersed IN are cooled down to a temperature where some fraction of them freezes, the ice fraction f_{ice}.

The majority of modern ice nucleation instruments measures this fraction of ice particles f_{ice} as a function of temperature, size, and microphysical properties of IN. The value of f_{ice} is a measure for the freezing ability of supercooled droplets and, furthermore, can be used in a parameterization of IN activity for various aerosol particles. The ability to measure this property correctly depends strongly on the ability of a particle counting instrument to distinguish between liquid droplets and ice particles. This is

AMTD
5, 5753–5785, 2012

typically done by optical means, exploiting the fact that at water saturation ice crystals grow faster than liquid droplets thus making a simple size-threshold based segregation of detected particles possible (Rogers, 1988; Wagner et al., 2009).

In recent immersion freezing measurements with the Leipzig Aerosol and Cloud Interaction Simulator (LACIS) described in Niedermeier et al. (2010, 2011), the commercial white light optical particle counter (WELAS® 1000, Palas®, Karlsruhe, Germany) was used for the determination of the ice fraction. In these experiments, LACIS was operated in a mode where the non-frozen supercooled droplets evaporated leaving ice and dry particles at the outlet of the flow tube. If the dry aerosol particles are much smaller than the ice particles, the latter can be clearly distinguished from the dry particles and so f_{ice} can be calculated. In certain situations, however, the dry aerosol particles have a broad size distributions overlapping with the size distribution of ice particles. The only way to resolve such a mixture is to allow the coexistence of ice particles and water droplets and to apply a different method to separate both populations of particles. This is a challenging task when both water droplets and ice particles have approximately the same optical size making the size-based separation impossible.

In this case, the geometrical difference between the highly spherical liquid droplets and the non-spherical ice particles has to be exploited. The most common approach is based on the fact that light scattered by spherical particles in the near-backward direction preserves its polarization state, while non-spherical particles change the state of polarization depending on the particle shape and orientation. This technique has been successfully used in remote sensing applications, for example, in lidar polarimetric measurements of ice and mixed-phase clouds, e.g. in Sassen (1991) and Seifert et al. (2010).

Studying the scattering of polarized light on non-spherical particles (spheroids), Mishchenko and Sassen (1998) and Zakharova and Mishchenko (2000) have shown that even a small increase of the aspect ratio and, therefore, a small deviation of the particle from the spherical shape can lead to a significantly large increase of the depolarization ratio. At the same time, no systematic dependence of the depolarization ratio

AMTD
5, 5753–5785, 2012

on the degree of non-sphericity has been found. Taking into account the variability of ice crystal habits in the atmospheric clouds (Bailey and Hallett, 2009), the applicability of the polarimetric approach has to be demonstrated in practice. Until now, only few in-situ instruments exist using the measurement of the polarization state of the scattered light for the discrimination of ice and water in laboratory and field experiments (Bundke et al., 2008; Krämer et al., 2009; Wagner et al., 2009; Nicolet et al., 2010).

Due to the small scattering intensity in backward direction, measuring the light scattered by a freely falling single droplet or ice particle into the backward direction is a very challenging task. Motivated by the need to build an optical instrument capable of counting ice particles in a system containing both liquid and frozen droplets of similar sizes, and trying to avoid the complications connected with the measuring of light scattered into the near-backward direction, we have investigated, both experimentally and theoretically by numerical calculations, the possibility of using the polarimetric measurements of light scattered in the near-forward direction.

In the following, we show the development of the Thermo-stabilized Optical Particle Spectrometer for the detection of Ice (TOPS-Ice) coupled with LACIS. The differentiation algorithm, which uses the pulse width of the cross-polarized scattering pulse of a particle streaming out of LACIS, will be explained and verified with theoretical calculations of the scattering intensity for different particle types.

2 Experimental setup

In the following section, the experimental setup for the immersion freezing experiments is described. The particle conditioning, i.e. the generation of droplets with a single immersed solid particle and the freezing of these droplets, takes place in the cloud simulator LACIS, which is described in Sect. 2.1. The optical particle spectrometer, TOPS-Ice, which was developed to detect the particles at the outlet of LACIS, is described in Sect. 2.2.

AMTD
5, 5753–5785, 2012

2.1 LACIS

The heterogeneous ice nucleation experiments are performed in the laminar flow diffusion chamber LACIS, which is explicitly described in Stratmann et al. (2004) and Hartmann et al. (2011). LACIS is a 7 m long vertical flow tube with an internal diameter of 15 mm. Mobility-selected aerosol particles are fed into LACIS through the inlet located on top of the flow tube. The humidified aerosol flow is streaming along the tube with a flow velocity of 0.7 ms^{-1} forming an aerosol stream of 2 mm in diameter in the center of the tube, which is surrounded by particle free humidified sheath air. LACIS consists of seven one meter long separate sections. By adjusting the wall temperatures of the sections, a precise temperature and saturation profile can be established along the tube axis. As a result, all particles moving along the axis of the LACIS flow tube experience the same humidity and temperature conditions. In the experiments described in this section, LACIS was operated in immersion freezing mode, i.e. the seed particles were first activated to supercooled droplets, and then the droplets were cooled down to the temperature where some of them freeze. For a certain amount of these supercooled droplets, the immersed particles act as IN leading to heterogeneous ice nucleation and hence freezing of the droplet. The number of frozen droplets divided by the number of frozen and liquid droplets yields the ice fraction f_{ice}, which can be considered as the probability of heterogeneous freezing as a function of temperature, particle type, particle size, and time.

2.2 TOPS-Ice

To determine the fraction of ice particles in the presence of liquid droplets in LACIS we have developed TOPS-Ice (Thermo-Stabilized Optical Particle Spectrometer for Ice Measurements). The layout of the instrument is shown in Fig. 1. TOPS-Ice uses a diode pumped solid state continuous wave laser (LasNova 50 green GLK 3220 T01, LASOS Lasertechnik GmbH, Jena, Germany) with a wavelength of 532 nm and an output power of 20 mW as a light source. The laser beam has a Gaussian profile with a

AMTD
5, 5753–5785, 2012

width of 0.7 mm (FWHM) and emits linearly polarized light, vertically polarized (200:1) with respect to the scattering plane (the drawing plane in Fig. 1). The beam is enlarged to a width of 2 mm and flattened by a cylindrical lens to intensify the illumination within the sensitive volume thus the resulting beam is 2 mm in width and about 50 µm in height (see the discussion in Sect. 4.1). The purity in terms of linear polarization of the laser beam is ensured by means of a Glan-Thompson calcite polarizer (extinction ratio: 100 000:1). The laser beam is focused on the particles streaming out of LACIS. The particles move through the illuminated area and scatter the light into all directions; the transmitted laser beam is caught by a beam trap. The light scattered by individual particles is collected into the solid angle of 0.89 sr located around the scattering angle $\vartheta = 42.5^{\circ}$ and is detected by three different photomultiplier tubes (PMT). PMT A is located at a scattering angle of $(\vartheta = 42.5^{\circ}, \varphi = 180^{\circ})$, and PMT B and PMT C are located at an angle of $(\vartheta = 42.5^{\circ}, \varphi = 0)$, where ϑ is the scattering angle and φ is the azimuth angle. A non-polarizing beam splitter cube (1:1) within the optical pathway of PMT B allows the detection of light by a third detector, PMT C, within the same angular range. The three detectors possess therefore the same detector geometry. In front of PMT C, another Glan-Thompson polarizer transmits only the horizontally polarized component of the scattered light. Around the outlet of LACIS, an air tight optical cell is built, so that the laser light and the scattered light is coupled out and in, respectively, through a glass window. The cooling jacket of LACIS is protruding inside the optical cell ensuring that the temperature of the gas flow stays constant down to the sensitive volume (and explaining the "Thermo-stabilized" in the name of the instrument). Optical fibers with an aperture of $\beta = 25.4^{\circ}$ and a core diameter of 400 µm and 200 µm for PMT A and PMT B/C, respectively, are used to deliver the scattered light to the PMTs. The larger core diameter of the optical fiber allows for a larger field of view for PMT A as compared to PMT B/C, so that the sensitive volume, shaped by the intersection of the illumination beam and the field of view of PMT B/C, is embedded into the sensitive volume of PMT A. This is done to minimize edge zone errors. A particle is only counted as being "valid" if all detectors receive a signal at the same time to ensure that the

AMTD
5, 5753–5785, 2012

particle is situated completely within the sensitive volume caused by the intersection of the illumination beam and PMT A. To record and analyze the scattering pulses by the three detectors and to provide an almost real time validation of the measured signal, we use the fast data acquisition unit together with a LabVIEW based program package, as described in Kiselev et al. (2005).

The validated pulse amplitudes received from PMT A can then be used to retrieve the size distribution of the droplets. This is achieved by means of the instrument response function that is first calculated theoretically for the TOPS-Ice scattering geometry and then calibrated with monodisperse polystyrene latex microspheres (PSL, Duke Scientific Corp., Palo Alto, CA, USA) as described in Kiselev et al. (2005). An example of the response curve for TOPS-Ice is shown in Fig. 4 and will be discussed in Sect. 4.1. Although the curve is ambiguous and oscillates strongly, the uncertainty in the size determination is less than 0.5 µm for spherical particles.

The scattered light detected with PMT C is used to distinguish between frozen and unfrozen droplets. For the discrimination, the change of the polarization state of the incident light during the scattering process is used. The theoretical background is given in Sect. 3, while the applied differentiation algorithm based on the measurement of the pulse width of the scattered pulse is explained in Sect. 4.

3 Theory

Different approaches for the theoretical investigation of the scattering of ice particles with different habits have been developed, the most widely used being: geometric ray-tracing methods (Takano and Jayaweera, 1985; Macke et al., 1996), finite difference time domain method (FDTD) (Yang and Liou, 1996; Baran et al., 2001), T-Matrix approach (Mishchenko and Hovenier, 1995; Mishchenko and Sassen, 1998; Rother, 2009) and Discrete Dipole Approximation (DDA) (Draine and Flatau, 1994). Meanwhile, a wide database of computational programs exists for the theoretical investigation of the scattering behavior for diverse particle shapes (Wriedt and Hellmers, 2008).

AMTD
5, 5753–5785, 2012

For the following considerations, the components $P_{i,j}(\vartheta)$ of the Muller Matrix (van de Hulst, 1982; Bohren and Huffmann, 1983) with a resolution of $\Delta\vartheta = 1^\circ$ were calculated: for randomly oriented spheroids, with the T-Matrix method from the work package mieschka (Rother, 2009); for spherical particles, as a special case of the spheroids, Lorenz-Mie theory also from the work package mieschka was used. To be able to compare the results for particles with different shape, the volume equivalent size parameter x_{ve} is chosen as the characteristic size of the particles.

All data were calculated with a refractive index of $n = 1.33$, which corresponds to the refractive index of water at $\lambda = 532$ nm. We neglect the difference of the refractive indexes of water and ice ($n = 1.31$) since it is irrelevant for the main purpose of our examination.

We use linearly vertically polarized light, so that the Stokes vector for the incident light has the following form: $\boldsymbol{S}_i = (I_i, Q_i, U_i, V_i)^T = (1, -1, 0, 0)^T$. To calculate the scattered light at an arbitrary observation point on the detector, which is rotated into 42.5° scattering angle the effective Muller Matrix $\mathbf{F}(\vartheta, \varphi)$ has to be examined as described in Yang et al. (2003). The parameter ϑ describes the scattering angle and φ is the azimuth angle. The evaluation of $\mathbf{F}(\vartheta, \varphi)$ is done for discrete points in steps of $\Delta\vartheta = 1^\circ$ and $\Delta\varphi = 1^\circ$. The resulting Stokes vector for the scattered light $\boldsymbol{S}_s$ as a function of ϑ and φ can then be calculated by the following equation:

$$\boldsymbol{S}_s(\vartheta, \varphi) = \begin{pmatrix} I_s(\vartheta, \varphi) \\ Q_s(\vartheta, \varphi) \\ U_s(\vartheta, \varphi) \\ V_s(\vartheta, \varphi) \end{pmatrix} = \mathbf{F}(\vartheta, \varphi)\boldsymbol{S}_i. \quad (1)$$

The total scattering intensity as measured by PMT A and PMT B, equals to $I_s(\vartheta, \varphi)$. The horizontal component of the scattered intensity as measured by PMT C, which has a polarizer in front, is given by:

$$I_x(\vartheta, \varphi) = \frac{1}{2}\left(I_s(\vartheta, \varphi) + Q_s(\vartheta, \varphi)\right). \quad (2)$$

AMTD
5, 5753–5785, 2012

To derive the total measured intensity in the angular range of the detector PMT C I_C^d at $\vartheta = 42.5^\circ \pm 12.7^\circ$, the calculated intensity $I_x(\vartheta, \varphi)$ is integrated over the detector area. A similar approach can be taken to derive the intensity measured by the other detectors $I_{A,B}^d$ by integrating $I_s(\vartheta, \varphi)$ over the detector area.

The detector area can be considered as a circle on a sphere with arbitrary radius R. For simplification, we use $R = 1$ for the further geometrical considerations. The angles ϑ and φ from the scattering calculations are chosen as coordinates. The detector area is then located at $\vartheta_d = 42.5^\circ$ with an aperture of $\beta = 12.7^\circ$ from the center of the sphere. The radius of the detector area is then $R_d = \sin\beta$. From geometrical considerations, the condition for a point (ϑ, φ) on the sphere laying within the detector area A_d is given by:

$$0 > \sin^2\vartheta\cos^2\varphi\cos^2\vartheta_d - 2\sin\vartheta\cos\varphi\sin\vartheta_d(\cos\beta - \sin\vartheta\cos\varphi\cos\vartheta_d) + \\ + \tan^2\vartheta_d(\cos\beta - \sin\vartheta\cos\varphi\sin\vartheta_d)^2 + \sin^2\vartheta\sin^2\varphi - \sin^2\beta \quad (3)$$

As we use discrete values for ϑ and φ, the integral over the detector area has to be replaced with the summation over discretized values I_x for every (ϑ, φ) laying within the field of view of the detector, leading to the intensity I_C^d measured by PMT C:

$$I_C^d = \sum_{(\vartheta,\varphi)\subset A_d} I_x(\vartheta, \varphi)\Delta\vartheta\Delta\varphi\sin\varphi \quad (4)$$

To compare the actual signal detected by PMT C for spheres and spheroid particles with different aspect ratios ϵ, the intensity I_C^d from Eqs. (3) and (4) is calculated, shown in Fig. 2 for different volume equivalent size parameters x_{ve}. The considered spheroids have two axis of the same length a and one axis of length b. The aspect ratio ϵ is defined as the ratio b/a, so that aspect ratios of $\epsilon < 1$ represent oblate spheroids, and aspect ratios of $\epsilon > 1$ represent prolate spheroids. The axis on the top allows for conversion of the volume equivalent size parameter x_{ve} to the volume equivalent particle diameter d_{ve} for the used wavelength of 532 nm. The axis on the right shows what the calculated relative intensity on the detector approximately means in terms of the

AMTD
5, 5753–5785, 2012

voltage signal measured by PMT C. The conversion to the detector voltage signal is performed by a comparison of PMT A and PMT C with signals from water droplets, and PMT A was calibrated with spherical PSL particles with known diameter and refractive index. The figure reveals two main features: first, the cross polarized component of the light scattered by spherical particles is non-zero and therefore the presence of a signal in channel C can not be used as a single criteria for detecting the non-spherical particle; and second, the calculated detector response is significantly higher for the randomly oriented spheroids with an aspect ratio $\epsilon \neq 1$ than for a spherical particles ($\epsilon = 1$) of the same volume equivalent size. Besides, the figure shows a general increase of the signal for larger particles. In brief, assuming comparable sizes and no preferred orientation, a signal strength based differentiation between spherical and non-spherical particles is possible. Both assumptions (size similarity of the particle population and the absence of preferential orientation) used for this simulation are realistic for LACIS: the conditions inside the flow tube are well defined, thus every particle experiences the same saturation and temperature conditions resulting in similar droplet sizes at the outlet of LACIS, and, assuming the ice particles having only short time to grow and freeze at approximately the same time, similar ice particle sizes can be assumed; furthermore, for a flow velocity of $0.7\,\mathrm{m\,s^{-1}}$ no preferred orientation can be expected.

The difference between spherical and non spherical particles is further demonstrated in Fig. 3. Here, the intensity I_C^d on PMT C normalized by I_C^d of the sphere, is plotted over the volume equivalend size parameter x_{ve} for different aspect ratios ϵ. The signal of the spheroid particles is in average about factor 5 higher than for the spherical particles. Therefore, a clear differentiation between the spherical and non-spherical particles in random orientation is possible.

We have to admit, however, that calculating the orientation averaged scattering signal does not provide an ultimate proof that no particle in some *fixed* orientation would produce a signal comparable to that of a spherical particle having the same d_{ve}. Calculations of the response functions of spheroid particles in all *fixed* orientations are too time consuming and would not provide ultimate applicability proof either, considering

AMTD
5, 5753–5785, 2012

that the actual ice particles never exhibit rotational symmetry and that depolarization factor is nonlinearly dependent on the degree of deviation from an ideal sphere (Mishchenko and Sassen, 1998). Note also, that a distinction of particle shape (in terms of ϵ) is not possible with our ice droplet differentiation method.

In Fig. 4, the relative intensity integrated over the detector area that has no polarizer (PMT A/B) within the optical pathway is shown. In contrast to Fig. 2, the detector response hardly differs for different particle shapes. However, the close resemblance of the response functions for small ($x_{ve} < 20$) spherical and non-spherical particles suggests that the response function averaged over ϵ might be used for the determination of the particle size without introducing too strong shape dependent error.

4 Ice fraction determination with TOPS-Ice

During the first measurements of f_{ice} conducted with TOPS-Ice at LACIS, we have discovered that it is beneficial to use the width distribution and not the amplitude distribution of pulses recorded by PMT C for the droplet and ice particle size range investigated. In the following sections we will discuss the reason for this behavior and describe the realization of this approach for the retrieval of ice fractions. Furthermore, an immersion freezing experiment using Arizona Test Dust (ATD) particles was done with both TOPS-Ice and WELAS in order to compare the two measurement methods.

4.1 Using the pulse width of the scattering signal for the discrimination of droplets and ice particles

The analogue voltage signals from the three PMTs are digitized by a 14 Bit High-Speed Waveform Digitizer (USB3000, R-Technology Ltd) with a sampling rate of 1 MHz per detection channel and are recorded by the measurement computer. The validation algorithm is then applied to the recorded sequence of pulses. The raw pulse waveforms,

AMTD
5, 5753–5785, 2012

i.e. the recorded voltage signal from the detector versus time, generated by a scattering particle moving through the illuminated measurement volume, have an approximately Gaussian shape, reflecting the profile of the laser beam in vertical direction. The digital waveform is then smoothed by applying a filter with Gaussian kernel.

If the smoothed signal exceeds a preset trigger threshold L for the duration of some minimum time interval, the waveform is considered as a pulse and its parameters (entry time stamp, height, width, maximum signal position) are stored. The shape of a pulse waveform depends on the spatial distribution of the illumination intensity within the sensitive volume, the velocity and size of the particle, and the delay time of the electronics. For every valid signal pulse, the signal pulse height H and the signal pulse width W from all three detectors are stored. From these data, a pulse height distribution (PHD) and a pulse width distribution (PWD) for an ensemble of particles is recorded. The PHD of PMT A (from now on, PHD^A) is used to derive a size distribution of the particle ensemble. The PWD of PMT C (PWD^C) is used for the water-ice discrimination; this will be explained below.

To characterize the spatial distribution of the laser intensity in the sensitive volume of TOPS-Ice, we have placed a pin hole into the measurement volume (Fig. 5). The diffraction on the pin hole simulates the scattering of a particle. By displacing the pin hole along the x-, y- and z-axis, the illumination intensity within the measurement volume was determined by measuring the response on the different detectors as a function of the pin hole position. Following the method suggested by Schmidt et al. (2004), we recorded the three dimensional response signal distributions across the measurement volume for different pin hole diameters (from 50 µm to 200 µm), and extrapolated these intensity distributions towards the zero pin hole diameter. Summarizing, the signal profile across the sensitive volume in y-direction was found to have a Gaussian shape with a standard deviation $\sigma = 50$ µm for detector C. Note that this value is independent of the particle size.

The usage of the signal pulse width W as a measurement parameter instead of the signal pulse height H turned out to have some advantages in our special measurement

AMTD
5, 5753–5785, 2012

regime. Consider a signal pulse that has a Gaussian shape and hence can be described with the following formula:

$$P(t) = H \cdot \exp\left(-\frac{(t-t_0)^2}{2\sigma_p^2}\right), \quad (5)$$

where H is the signal pulse height, t_0 is the position of signal maximum on the time scale, and σ_p is the standard deviation in units of the time scale (µs). In Fig. 6, an ideal pulse waveform is shown. The values t_1 and t_2 are the solutions of the equation $P(t) - L = 0$, where L is the trigger threshold, and are given by the following equation:

$$t_{1,2} = \pm\sqrt{2\sigma_p^2 \log\frac{H}{L}} + t_0. \quad (6)$$

The pulse width W is defined as $W = t_2 - t_1$ and can be expressed as a function of pulse height H:

$$W_{L,\sigma}(H) = 2\sqrt{2\sigma_p^2 \log\frac{H}{L}}, \quad (7)$$

which is equivalent to:

$$H_{L,\sigma}(W) = L \exp\frac{1}{2\sigma^2}\left(\frac{W}{2}\right)^2. \quad (8)$$

Substituting the typical values $\sigma_p = 28$ µs and $L = 0.03$ V, the relation between H and W can be explicitly calculated (the blue line in Fig. 7). In Fig. 7, the theoretical relation between H and W is also compared to experimental results. The red data points show a statistics of the pulse height from an exemplary measurement with water droplets of different sizes. The red dots give the average pulse height for pulses having the same pulse width (measured with the 1 µs resolution), the error bars give the standard

AMTD
5, 5753–5785, 2012

deviation. The measured curve shows a general agreement with the theoretical relation (blue line from Eq. 8).

Due to the nonlinear form of the relationship between the pulse height and the pulse width (see Fig. 7), the form of the PWD is different from that of the PHD. For signal pulses smaller than 1 V, a small change in the pulse amplitude results in a relatively large change in the pulse width. In contrast, for larger particles (signal > 1 V), and, therefore, for larger pulse amplitudes, a relatively large difference in pulse amplitude results in a small variation of the pulse width. For bimodal distribution of pulse amplitudes (encountered in a typical ice nucleation experiment, later shown in Fig. 8), this leads to a broadening of the droplet mode and a more compact ice mode. For even larger droplets and ice particles, it is possible to reduce the amplification of the PMTs so that the signal lay within the suitable range of about 1 V.

To illustrate typical measurements with TOPS-Ice for droplets and ice, three examples are given in Fig. 8. The panels (a) and (b) show the PHD measured with PMT C (PHD^C) and the PWD^C for the droplet ensembles, respectively, obtained from an experiment where 200 nm ammonium sulfate particles activated to droplets of an approximate size of 2 µm. In this example, one narrow droplet mode exists both in PHD^C and PWD^C. However, the PHD^C in the panel (a) is poorly resolved, whereas PWD^C in the panel (b) shows a well resolved main mode corresponding to the droplets and a shoulder on left side of the droplet peak resulting from the droplets crossing the sensitive volume inside the edge zone. This resulting edge zone error is later considered as a measurement uncertainty.

The panels (c) and (d) show the PHD^C and the PWD^C for a particle ensemble consisting of only ice particles. In this particular experiment, the liquid droplets activated on the mineral dust particles (Arizona Test Dust (ATD), ISO 12103-1, A1 Ultrane Test Dust, Powder Tech- nology Inc., Burnsville, Minnesota, USA) froze at temperature of −40 °C, due to either heterogeneous or homogeneous ice nucleation. Both the PHD^C and PWD^C are very broad and show a clear single mode.

AMTD
5, 5753–5785, 2012

The panels (e) and (f) show, respectively, the PHD^C and the PWD^C for a mixed ensemble of droplets and ice particles, formed on the 300 nm ATD particles at −35 °C. The characteristic size of ice particles in this example is similar to the size of the particles in the "ice only" experiment (panels c, d) and the size of the droplets in the mixture is similar to that of the "droplet only" experiment (panels a, b). Therefore, both the ice mode and the droplet mode are located in the similar range of magnitudes compared to the "ice only" and "droplet only" experiments. As a result, the PWD^C shows two clearly distinguishable modes whereas the PHD^C exhibits a narrow droplet mode and inhomogeneously scattered discrete values corresponding to ice particles. This mode separation suggests an advantage of using the PWD^C for the retrieval of ice fraction in the mixed-phase experiments. Finally, the number of droplets and ice particles can be obtained and the ice fraction f_{ice} can be reliably calculated by an algorithm explained in Sect. (4.2).

4.2 Evaluation of the TOPS-Ice data

In the following, the calculation of the ice fraction from the PWD^C measured with TOPS-Ice is described in detail. The applicability of the method is demonstrated in two immersion freezing experiments with different resulting ice fractions performed at LACIS.

First, a digital low pass filter with Hamming window is applied to the PWD. The resulting smoothed PWD is shown by the black line in Fig. 9. Next, the following iteration procedure is applied to the data: at initial step, a normal distribution with parameter N_0, σ_0 and μ_0 is fitted to the droplet mode of the smoothed PWD, where N_0 is the area under the curve, σ_0 is the standard deviation and μ_0 is the mean value of the normal distribution (similar to Eq. 5). To ensure that the droplet mode, and not the ice mode, is used for the fit, at initial step, the data range is manually constrained to the droplet mode. For every next iteration step n, only a limited range W_n of the PWD data is considered:

$$\mu_{n-1} - k\,\sigma_{n-1} < W_n < \mu_{n-1} + l\,\sigma_{n-1}, \tag{9}$$

AMTD
5, 5753–5785, 2012

where μ_{n-1} and σ_{n-1} are taken from the previous iteration fit and the two parameters k and l are set by default to 1.5, which mostly lead to a good agreement of the fitting curves to the filtered data. After limitation of the data to W_n, a new fit with parameters N_n, σ_n and μ_n is applied.

If $\sigma_n - \sigma_{n-1} \leq 0.0001$, the iteration is stopped, the number of droplets N_d is set to N_n, and $\sigma_d = \sigma_n$ and $\mu_d = \mu_n$ are the parameters of the droplet mode (red line in Fig. 9). This iteration algorithm ensures that the normal distribution fit is applied to the droplet mode only.

Next, the fitted droplet mode is subtracted from the smoothed PWD thus leaving a residual data shown by the blue line in Fig. 9. The residual data shows two major modes. The mode on the right side is assumed to be produced by the ice particles, and is used for the calculation of the ice fraction f_{ice}. The mode on the left side is caused by the edge zone counts coming from ice and droplets; the number of these counts N_f allows us to estimate the error of ice fraction f_{ice}. Nevertheless, there is also an error of the fitting algorithm, which is about 0.5 for very small f_{ice} (< 0.01), and get less for higher ice fractions.

The number of ice particles N_i is determined by summing up over the ice mode of the residual data. The ice fraction f_{ice} is then given by:

$$f_{ice} = \frac{N_i}{N_d + N_i}. \tag{10}$$

The absolute error from the edge zone error counts is N_f. Having no information about what fraction of edge zone error counts is coming from what particle mode, we take N_f as an upper estimate for the absolute error for the number of unfrozen droplets as $\Delta N_d = N_f N_d/(N_d + N_i)$ and as an upper estimate of the absolute error for the number of ice particles as $\Delta N_i = N_f N_i/(N_d + N_i)$. This approach gives us an upper estimate of the relative error of f_{ice} in the following form:

$$\frac{\Delta f_{ice}}{f_{ice}} = \frac{2N_f N_d}{(N_d + N_i)^2}. \tag{11}$$

AMTD
5, 5753–5785, 2012

This method was applied to extract the f_{ice} values from the measurements done with TOPS-Ice installed underneath LACIS, where 300 nm ATD particles were activated to droplets which were frozen. The values of f_{ice} obtained with the two different optical instruments (WELAS, as descibed in Niedermeier et al. (2010), and TOPS-Ice (this paper)) are compared in Fig. 10.

During the measurements where TOPS-Ice was used for the determination of f_{ice}, LACIS was run in the modus where droplets and ice particles coexist at the outlet of the LACIS flow tube. The resulting ice fraction is shown as red diamonds. In contrast, for the measurements with WELAS (blue squares in Fig. 10), LACIS was run in a modus where the liquid droplets have been evaporated before reaching the end of the flow tube. The two modi differ in a different due point adjusted at the inlet of the tube which results in either droplets and ice particles (measurement with TOPS-Ice) or dry dust particles and ice particles (measurement with WELAS) at the outlet of LACIS. The error bars of the TOPS-Ice data show the experimental uncertainties resulting from the edge zone counts, as explained above. The error bars of the WELAS data are the doubled standard deviation taken from different measurements. Although LACIS was run in two different modi and two completely different optical methods for the detection were used, the figure shows an excellent agreement of both measurement results.

5 Conclusions

An optical single-particle counter TOPS-Ice was developed to satisfy the need for reliable determination of the ice particle fraction in mixed particle ensembles consisting of liquid droplets and ice particles of similar size. Additionally, the instrument allows the measurement of the particle sizes independently of their phase state. The applicability of the method has been demonstrated in the experiment conducted at the laminar flow diffusion chamber LACIS.

The differentiation between liquid and frozen droplets is based on the measurement of the cross-polarized component of the scattered light. Although for the chosen

AMTD
5, 5753–5785, 2012

scattering geometry ((42.5 ± 12.7)° from the forward direction) the cross-polarized linear component of the light scattered by spherical droplets is not completely suppressed (which is only possible for true backscattering), the non-sphericity of ice particles results in a stronger scattering signal, which can be employed for the differentiation of ice and droplet modes.

To support these experimental findings, we have used the T-Matrix method to calculate the scattering intensities for the ensembles of ellipsoids of variable aspect ratio in random orientation with account for the actual scattering geometry and optical properties of ice. We show that the scattering intensity of a spherical particle in the depolarization channel is weaker than for the non-spherical particles and can be used for the differentiation. However, such differentiation is only valid for the statistically large mixed ensembles of spherical droplets and randomly oriented ice particles.

The usage of the scattering signal pulse width W of the depolarization channel as a measurement parameter instead of the signal pulse amplitude turned out to be advantageous in our measurement regime. Exploiting the non-linear relationship between pulse width and pulse amplitude, we show that for a mixed particle ensemble the distribution of the signal pulse width measured in the depolarization channel always has two modes: one for the liquid water droplets and one for the ice particles. Assuming that the ice particle mode always corresponds to the pulses with higher amplitudes and therefore greater width, and applying a Gaussian fit routine to the two modes, both the number of liquid droplets and ice particles, and consequently f_{ice}, can be determined.

To verify the applicability of this approach, we have used the TOPS-Ice for the measurement of fractions of frozen droplets as a function of temperature in the immersion freezing experiment in LACIS. The values obtained with TOPS-Ice and the data evaluation algorithm developed were compared with results obtained from a different optical instrument, the white light optical particle counter WELAS, as described in Niedermeier et al. (2010). Both methods show an excellent agreement although LACIS was run in two different operation modi and the optical detection methods were completely different.

AMTD
5, 5753–5785, 2012

However, the measuring principle of the newly developed TOPS-Ice instrument has certain advantages as compared to the WELAS instrument. In the WELAS-based measurements, the droplets have to be evaporated within LACIS, so that only small aerosol particles and large ice particles reach the optical detection section at the outlet of the flow tube. In case of large or strongly polydisperse aerosol particles, the dry aerosol mode is overlapping with the ice particle mode making the mode separation not possible. In such situation, allowing the coexistence of droplets an ice particles at the LACIS outlet and applying the depolarization-based detection method is the only and better way to separate the modes and to enable the f_{ice} determination.

Acknowledgements. This work was partly funded by the German Science Foundation (DFG) under contract HE 939/21-1. Additionally, this work was financially supported by the research project EUROCHAMP II.

References

Ansmann, A., Tesche, M., Althausen, D., Muller, D., Seifert, P., Freudenthaler, V., Heese, B., Wiegner, M., Pisani, G., Knippertz, P., and Dubovik, O.: Influence of Saharan dust on cloud glaciation in southern Morocco during the Saharan Mineral Dust Experiment, J. Geophys. Res.-Atmos., 113, D04210, doi:10.1111/j.1600-0889.2008.00384.x, 2008. 5755

Bailey, M. and Hallett, J.: A comprehensive habit diagram for atmospheric ice crystals: Confirmation from the laboratory, AIRS II, and other field studies, J. Atmos. Sci., 66, 2888–2899, 2009. 5757

Baran, A. J., Yang, P., and Havemann, S.: Calculation of the single-scattering properties of randomly oriented hexagonal ice columns: a comparison of the T-matrix and the finite-difference time-domain methods, Appl. Opt., 40, 4376–4386, 2001. 5760

Bohren, C. F. and Huffmann, D. R.: Absorption and Scattering of Light by Small Particles, Wiley, 1983. 5761

Bundke, U., Nillius, B., Jaenicke, R., Wetter, T., Klein, H., and Bingemer, H.: The fast Ice Nucleus chamber FINCH, Atmos. Res., 90, 180–186, Sp. Iss. SI, 2008. 5755, 5757

Cantrell, W. and Heymsfield, A.: Production of ice in tropospheric clouds – A review, B. Am. Meteorol. Soc., 86, 795–807, 2005. 5754

AMTD

5, 5753–5785, 2012

Connolly, P. J., Möhler, O., Field, P. R., Saathoff, H., Burgess, R., Choularton, T., and Gallagher, M.: Studies of heterogeneous freezing by three different desert dust samples, Atmos. Chem. Phys., 9, 2805–2824, doi:10.5194/acp-9-2805-2009, 2009. 5755

de Boer, G., Morrison, H., Shupe, M., and Hildner, R.: Evidence of liquid dependent ice nucleation in high-latitude stratiform clouds from surface remote sensors, Geophys. Res. Lett., 38, L01803, doi:10.1029/2010GL046016, 2011. 5755

Draine, B. and Flatau, P.: Discrete-dipole approximation for scattering calculations, J. Opt. Soc. Am. A, 11, 1491–1499, 1994. 5760

Hartmann, S., Niedermeier, D., Voigtländer, J., Clauss, T., Shaw, R. A., Wex, H., Kiselev, A., and Stratmann, F.: Homogeneous and heterogeneous ice nucleation at LACIS: operating principle and theoretical studies, Atmos. Chem. Phys., 11, 1753–1767, doi:10.5194/acp-11-1753-2011, 2011. 5755, 5758

Hoose, C., Kristjánsson, J., Chen, J., and Hazra, A.: A Classical-Theory-Based Parameterization of Heterogeneous Ice Nucleation by Mineral Dust, Soot, and Biological Particles in a Global Climate Model, J. Atmos. Sci., 67, 2483–2503, 2010. 5755

Kiselev, A., Wex, H., Stratmann, F., Nadeev, A., and Karpushenko, D.: White-light optical particle spectrometer for in situ measurements of condensational growth of aerosol particles, Appl. Opt., 44, 4693–4701, 2005. 5760

Krämer, M., Meyer, J., Afchine, A., Newton, R., Baumgardner, D., and Schnaiter, M.: HALO ice crystal spectrometer intercomparison at the AIDA – chamber: first results from the novel ice experiment NIXE-CAPS, in: EGU General Assembly 2009, Vol. 11, 2009. 5757

Macke, A., Mueller, J., and Raschke, E.: Single scattering properties of atmospheric ice crystals, J. Atmos. Sci., 53, 2813–2825, 1996. 5760

Mishchenko, M. I. and Hovenier, J. W.: Depolarization of Light Backscattered by Randomly Oriented Nonspherical Particles, Opt. Lett., 20, 1356–1358, 1995. 5760

Mishchenko, M. I. and Sassen, K.: Depolarization of lidar returns by small ice crystals: An application to contrails, Geophys. Res. Lett., 25, 309–312, 1998. 5756, 5760, 5764

Nicolet, M., Stetzer, O., Lüönd, F., Möhler, O., and Lohmann, U.: Single ice crystal measurements during nucleation experiments with the depolarization detector IODE, Atmos. Chem. Phys., 10, 313–325, doi:10.5194/acp-10-313-2010, 2010. 5757

Niedermeier, D., Hartmann, S., Shaw, R. A., Covert, D., Mentel, T. F., Schneider, J., Poulain, L., Reitz, P., Spindler, C., Clauss, T., Kiselev, A., Hallbauer, E., Wex, H., Mildenberger, K., and Stratmann, F.: Heterogeneous freezing of droplets with immersed mineral dust

AMTD
5, 5753–5785, 2012

particles – measurements and parameterization, Atmos. Chem. Phys., 10, 3601–3614, doi:10.5194/acp-10-3601-2010, 2010. 5756, 5770, 5771, 5785
Niedermeier, D., Hartmann, S., Clauss, T., Wex, H., Kiselev, A., Sullivan, R. C., DeMott, P. J., Petters, M. D., Reitz, P., Schneider, J., Mikhailov, E., Sierau, B., Stetzer, O., Reimann, B., Bundke, U., Shaw, R. A., Buchholz, A., Mentel, T. F., and Stratmann, F.: Experimental study of the role of physicochemical surface processing on the IN ability of mineral dust particles, Atmos. Chem. Phys., 11, 11131–11144, doi:10.5194/acp-11-11131-2011, 2011. 5756, 5785
Pruppacher, H. R. and Klett, J. D.: Microphysics of Clouds and Precipitation, Kluwer Academic Publishers, Dordrecht, The Netherlands, 1997. 5755
Rogers, D.: Development of a continuous flow thermal gradient diffusion chamber for ice nucleation studies, Atmos. Res., 22, 149–181, 1988. 5755, 5756
Rother, T.: Electromagnetic Wave Scattering on Nonspherical Particles: Basic Methodology and Simulations, Springer Berlin Heidelberg, 2009. 5760, 5761
Sassen, K.: The Polarization Lidar Technique for Cloud Research – a Review and Current Assessment, B. Am. Meteorol. Soc., 72, 1848–1866, 1991. 5756
Schmidt, S., Lehmann, K., and Wendisch, M.: Minimizing instrumental broadening of the drop size distribution with the M-Fast-FSSP, J. Atmos. Ocean. Technol., 21, 1855–1867, 2004. 5765
Seifert, P., Ansmann, A., Mattis, I., Wandinger, U., Tesche, M., Engelmann, R., Müller, D., Pérez, C., and Haustein, K.: Saharan dust and heterogeneous ice formation: Eleven years of cloud observations at a central European EARLINET site, J. Geophys. Res.-Atmos., 115, D20201, doi:10.1029/2009JD013222, 2010. 5756
Stetzer, O., Baschek, B., Lüönd, F., and Lohmann, U.: The Zurich Ice Nucleation Chamber (ZINC) – A new instrument to investigate atmospheric ice formation, Aerosol Sci. Technol., 42, 64–74, 2008. 5755
Stratmann, F., Kiselev, A., Wurzler, S., Wendisch, M., Heintzenberg, J., Charlson, R. J., Diehl, K., Wex, H., and Schmidt, S.: Laboratory studies and numerical simulations of cloud droplet formation under realistic supersaturation conditions, J. Atmos. Ocean. Technol., 21, 876–887, 2004. 5755, 5758
Takano, Y. and Jayaweera, K.: Scattering Phase Matrix for Hexagonal Ice Crystals Computed from Ray Optics, Appl. Opt., 24, 3254–3263, 1985. 5760
van de Hulst, H. C.: Light Scattering by Small Particles, Dover Pubn Inc, 1982. 5761

AMTD
5, 5753–5785, 2012

Wagner, R., Linke, C., Naumann, K. H., Schnaiter, M., Vragel, M., Gangl, M., and Horvath, H.: A review of optical measurements at the aerosol and cloud chamber AIDA, J. Quant. Spectrosc. Ra., 110, 930–949, 2009. 5755, 5756, 5757

Wiacek, A., Peter, T., and Lohmann, U.: The potential influence of Asian and African mineral dust on ice, mixed-phase and liquid water clouds, Atmos. Chem. Phys., 10, 8649–8667, doi:10.5194/acp-10-8649-2010, 2010. 5755

Wriedt, T. and Hellmers, J.: New Scattering Information Portal for the light-scattering community, J. Quant. Spectrosc. Ra., 109, 1536–1542, 2008. 5760

Yang, P. and Liou, K.: Finite difference time domain method for light scattering by small ice crystals in three-dimensional shape, J. Opt. Soc. Am. A, 13, 2072–2085, 1996. 5760

Yang, P., Wei, H. L., Kattawar, G. W., Hu, Y. X., Winker, D. M., Hostetler, C. A., and Baum, B. A.: Sensitivity of the backscattering Mueller matrix to particle shape and thermodynamic phase, Appl. Opt., 42, 4389–4395, 2003. 5761

Zakharova, N. T. and Mishchenko, M. I.: Scattering properties of needlelike and platelike ice spheroids with moderate size parameters, Appl. Opt., 39, 5052–5057, 2000. 5756

AMTD

5, 5753–5785, 2012

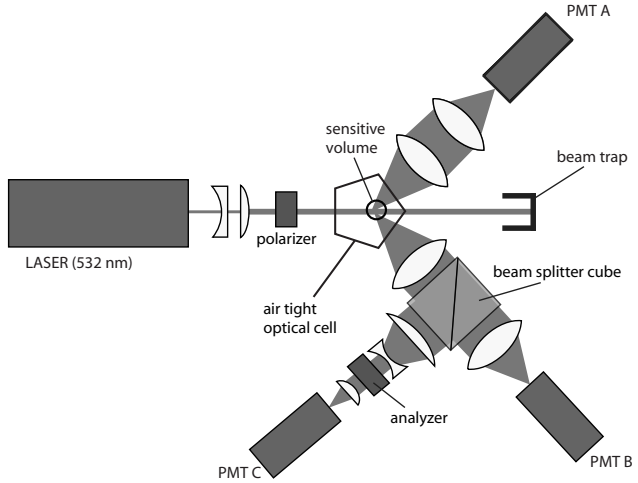

Fig. 1. Optical layout of TOPS-Ice (top view).

AMTD
5, 5753–5785, 2012

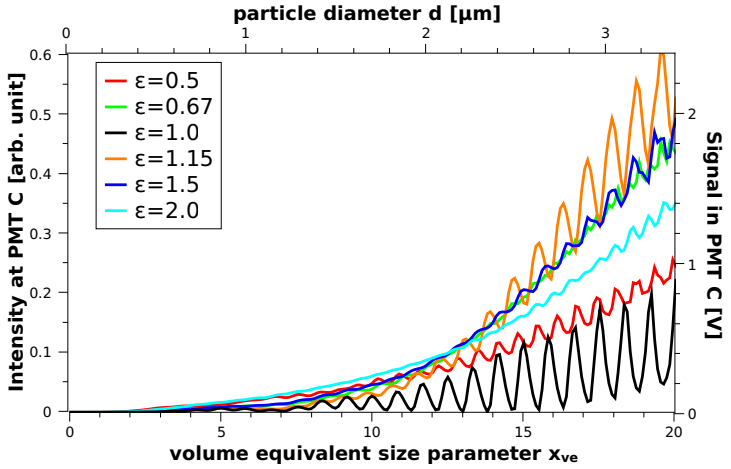

Fig. 2. Intensity integrated over the detector area (PMT C) I_C^d versus volume equivalent size parameter x_{ve} for randomly oriented spheroids with different aspect ratios ϵ. The axis at the top shows the particle diameter. The axis at the right shows the measured signal voltage in PMT C.

AMTD
5, 5753–5785, 2012

The discrimination of frozen and liquid droplets

T. Clauss et al.

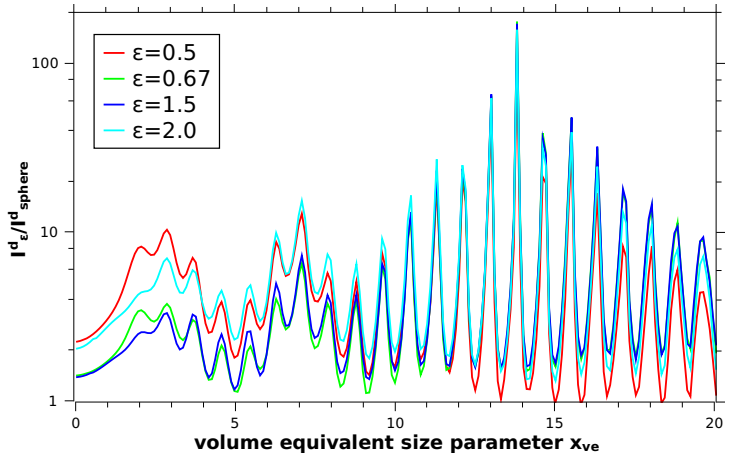

Fig. 3. Intensity on detector area (PMT C) I_C^d from randomly oriented spheroids normalized by I_C^d from sphere volume equivalent size parameter x_{ve} for different aspect ratios ϵ.

AMTD
5, 5753–5785, 2012

The discrimination of frozen and liquid droplets

T. Clauss et al.

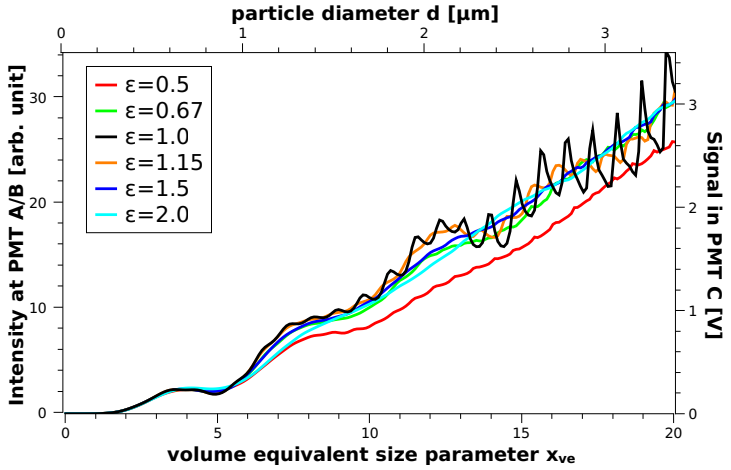

Fig. 4. Intensity integrated over the detector area without a polarizer within the optical pathway (PMT A/B) $I^{d}_{A/B}$ versus volume equivalent size parameter x_{ve} for orientation averaged spheroids with different aspect ratios ϵ.

AMTD
5, 5753–5785, 2012

The discrimination of frozen and liquid droplets

T. Clauss et al.

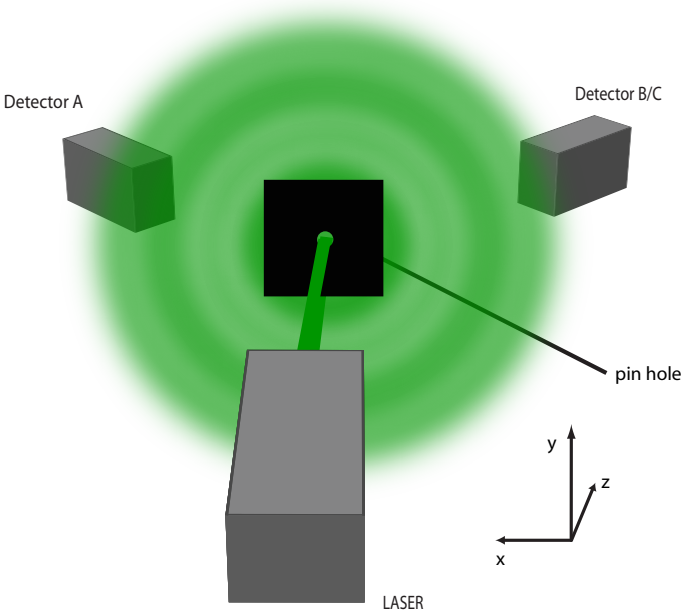

Fig. 5. The experimental setup for the measuring of the sensitive volume. The diffraction on the aperture simulates the scattering on a particle. The aperture can be displaced precisely along the x-, y- or z-axis.

AMTD
5, 5753–5785, 2012

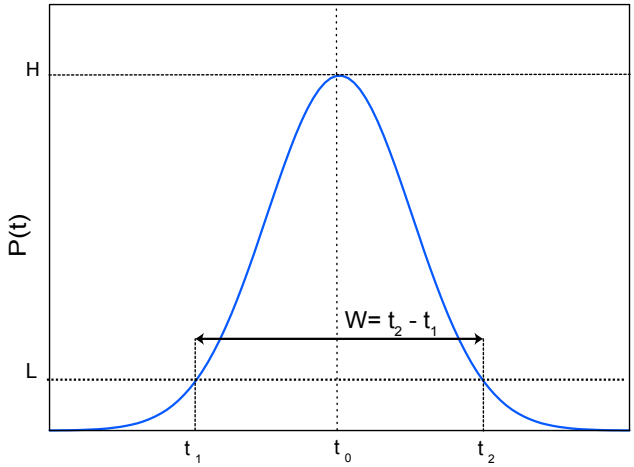

Fig. 6. Waveform of an ideal signal pulse. Parameter described in text.

AMTD
5, 5753–5785, 2012

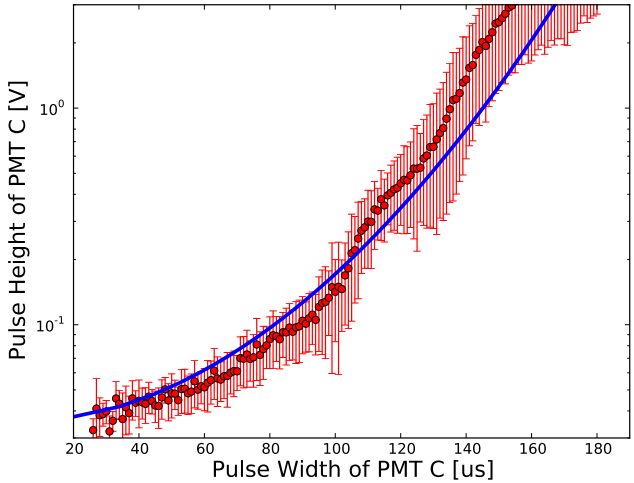

Fig. 7. Pulse width vs. pulse height for $\sigma_p = 28\,\mu s$ and $L = 0.03\,V$ (blue line) and data from a measurement with water droplets of different sizes (red dots give the average pulse height for the pulses h aving the same width, error bars give the standard deviation).

AMTD
5, 5753–5785, 2012

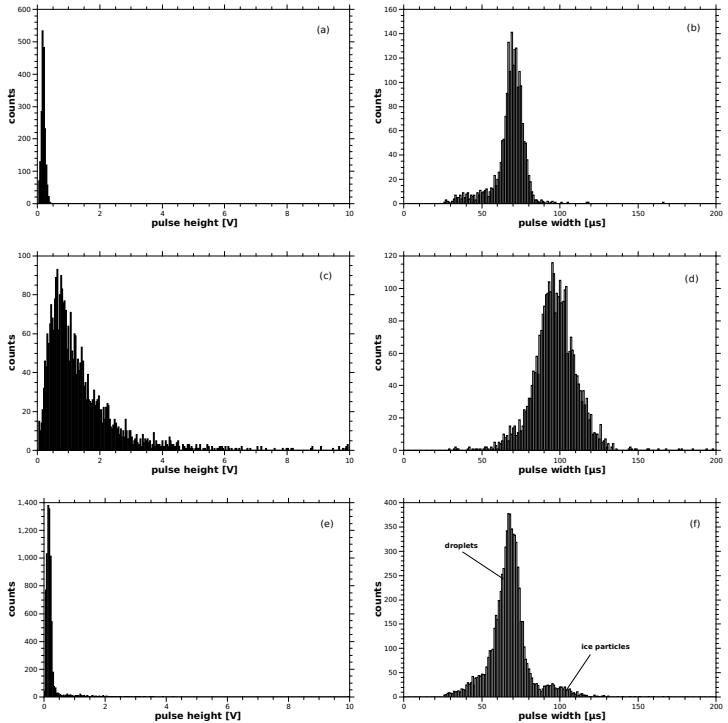

Fig. 8. Pulse height (left column) and pulse width (right column) distributions recorded in channel C for different particle populations. Panels **(a, b)**, show the distributions measured for the population of monodisperse droplets of apprimately 2 µm in diameter. Panels **(c, d)** show the distributions recorded for ice particles formed as a result of droplets freezing at −40 °C. The panels **(e, f)** show the distributions produced by a mixed particle ensemble of liquid and frozen droplets formed on 300 nm Arizona Test Dust (ATD) particles at −35 °C.

AMTD
5, 5753–5785, 2012

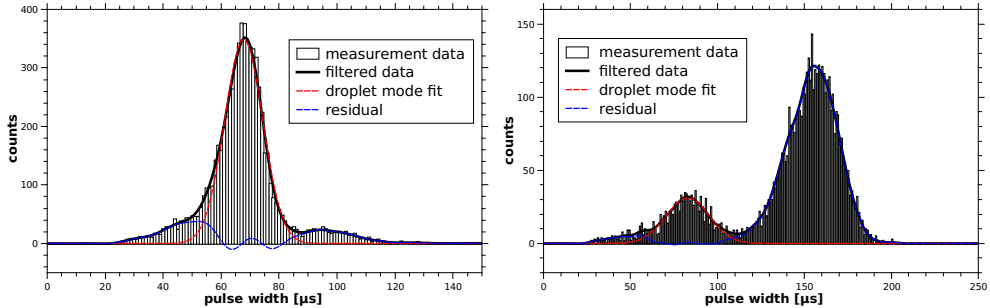

Fig. 9. TOPS-Ice data evaluation algorithm for two different ice fractions, f_{ice} = 0.06 on left panel (example from Fig. 5f), f_{ice} = 0.82 on right panel.

AMTD
5, 5753–5785, 2012

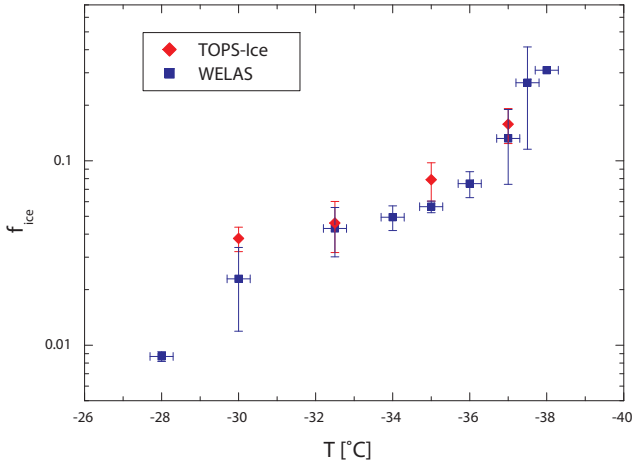

Fig. 10. Comparison of the ice fraction vs. freezing temperature determined with WELAS (Niedermeier et al., 2010, 2011) and with TOPS-Ice. 300 nm Arizona Test Dust particles were used for both measurements.

AMTD
5, 5753–5785, 2012